Mechanism insights for efficient photocatalytic reforming of formic acid with tunable selectivity: Accelerated charges separation and spatially separated active sites

Xiaoyuan Ye [1], Yuchen Dong [1], Ziying Zhang, Wengao Zeng, Tuo Zhang, Feng Liu, Xiangjiu Guan [*], Liejin Guo [*]

International Research Center for Renewable Energy, State Key Laboratory of Multiphase Flow in Power Engineering, Xi'an Jiaotong University, Xi'an 710049, China

ARTICLE INFO

ABSTRACT

Photocatalytic reforming of formic acid (FA) is considered a promising energy conversion method for producing solar fuels and valuable chemical feedstocks to achieve the carbon-neutral goal. However, the application of FA photocatalytic reforming has been restricted by the low efficiency and relatively fixed selectivity due to limited knowledge about the reaction mechanism. Herein, we study the efficient CdS/W_2N_3 photocatalyst system for photoreforming of FA with tunable selectivity to realize the conversion of products from H_2 to syngas under simulated sunlight. Widely tunable $CO:H_2$ ratios between 0 and 2.18 along with a record-high apparent quantum yield (AQY) of 61.00% (H_2) and 76.84% (syngas) at 420 nm have been demonstrated. Both theoretical investigation and experimental results show that intrinsic N vacancies and spatially separated active sites are vital factors in achieving tunable selectivity. This work provides a insightful information to construct and understand the photocatalytic system for efficiently reforming of FA with tunable selectivity.

1. Introduction

The urgency of carbon neutrality has sharply increased the demand for production and utilization of renewable energy, such as hydrogen energy, to reduce carbon emissions as much as possible. Formic acid (HCOOH, FA), with a high content of hydrogen (H_2, 4.4 wt%), is an ideal energy storage material, which is even superior to commercial Li-ion batteries in the aspect of gravimetric energy density [1–4]. Hydrogen production from FA via dehydrogenation process (HCOOH→H_2 +CO_2), with FA further regenerated from the carbon dioxide (CO_2) byproduct [5–8] or produced from biomass conversion [9,10], promises advantages of low-carbon emission, hence is beneficial for creating a carbon-neutral cycle. Solar-dirven photoreforming has received a great deal of attention as a green solar energy conversion technology used for FA reforming at room temperature [11,12]. Many potential catalysts are using to study the efficient reforming FA, such as MOF, [13] semiconductor, [14] organic polymer,[15] and single-atom catalysts [16–18]. Typically, CdS has been considered as a potential candidate semiconductor catalyst for photoreforming of FA due to its low cost,

appropriate redox capacity, and the special structure features, and high photocatalytic activity [19–21]. And the cocatalysts could further enhance the acticity and stable of the photocatalysts. Due to the excellent catalytic performance of the noble metal cocatalyst, a large number of cocatalysts [12], such as Ir−Ru complexes [22], Pd [23], Pt [24], AuPd [25], and AgPd [26], were investigated for FA reforming. However, considering the rarity and high cost of noble metals, noble-metal-free photocatalytic systems are more desirable for potential large-scale applications. In this regard, a CdS/CoP@RGO hybrid catalyst is reported to reach an H_2 production rate of 182 μmol·mg^{-1}·h^{-1} in FA aqueous solution with the apparent quantum yield (AQY) of 32% at 420 nm [27], and FeP@CdS nanorods (NRs) catalyst exhibits an AQY of 54% at 420 nm with the assistance of sodium formate (SF) [14]. Although the activity of hydrogen production from the above catalytic systems is remarkable, there is still much room for improvement in efficiency.

Beyond producing pure hydrogen, FA could also serve as a great source of carbon monoxide (CO, 60 wt%), which is a valuable raw chemical in the chemical industry, [28] via FA dehydration process (HCOOH→H_2O+CO). Additionally, a mixture of CO and H_2 (known as

syngas) could be theoretically produced from FA reforming, and further used for the synthesis of high-valued chemicals by the Fischer-Tropsch process [29–32]. Thus, the sustainable production of CO or syngas from FA has received attention. As one of the excellent examples, CdS quantum dots photocatalysts achieve highly active CO production and controlled generation of either H_2 or CO in FA at ambient conditions [33]. However, to our best knowledge, the existing researches for syngas production from FA photoreforming systems remain disjointed with respect to controllable selectivity. A recent example is Fe salen/CdS NRs catalyst that demonstrates syngas production by FA photoreforming with hydrogen selectivity changing at pH values between 3.2 and 6.0, whereas the variation range of CO/H_2 ratios is still relatively small (0.41–0.60) [34]. Although those above CdS-based photocatalytic reforming FA systems achieved excellent performance, for tunable selectivity of photoreforming of FA, a deeper insight into the mechanisms including the identification of intermediates and active sites is needed, based on which an efficient, low-cost, and selectively controllable photocatalytic system for FA reforming could be developed. It could provide a more flexible approach for FA to hydrogen or syngas production applications. In particular, a detailed study of active sites could provide ideas for further design of excellent photoreforming of FA systems for syngas production with tunable selectivity.

Herein, we report a photocatalytic system constructed with 1D CdS/ 2D W_2N_3 heterojunctions for the efficient reforming of FA. Notably, this noble-metal-free catalytic system provides controlled selectivity of products from pure hydrogen to syngas with consecutively tunable CO/H_2 ratios between 0 and 2.18, which is larger than the variation ranges of previous reports. A record-high apparent quantum yield (AQY) of 61.00% (H_2) and 76.84% (syngas) at 420 nm have been demonstrated. It is experimentally and theoretically demonstrated that both spatial separation of reduction active sites achieved in as-formed CdS/W_2N_3 heterojunction and production of the key intermediate (carbon dioxide radical anion, $CO_2^{\bullet-}$) contribute as crucial factors to realize selective photoreforming of FA, which promises a remarkable performance of H_2 and CO production superior to previous reports.

2. Materials and methods

2.1. Materials

All of the used materials were of analytical grade and used as received without further purification. Ethylenediamine (EDA), formic acid (HCOOH, ≥98%), ethanol absolute (C_2H_5OH, ≥99.7%), L-cysteine, cadmium acetate dihydrate (Cd(Ac)$_2$·2 H_2O), sodium hydroxide (NaOH), sodium formate (CHNaO$_2$), sodium tungstate dihydrate (Na$_2$WO$_4$·2 H_2O), tungsten trioxide (WO$_3$), and deuterium oxide (D$_2$O, Cambridge Isotope laboratories, Inc.) were purchased from Sinopharm Chemical Reagent Co., Ltd or Sigma Andrich. Ultrapure water (resistivity: ~18.5 MΩ·cm) was used when needed.

2.2. Methods

2.2.1. Preparation of 2D W_2N_3

The 2D layered W_2N_3 nanosheets were synthesized via a molten salt-directed synthesis method according to a modified literature method [35]. First, WO$_3$ powder and Na$_2$WO$_4$·2 H_2O powder (mole ratio of 1:1) were mixed via ball milling. in a planetary micro mill system (Fritsch PULVERISETTE 7 premium line) with a rotation speed of 400 rpm for 20 min (three cycles). Then, 100 mg of this mixture was put into a porcelain boat uniformly. The 2D W_2N_3 material was produced by annealing the as-prepared precursor at 750 °C for 5 h at the ramp rate of 1 °C min^{-1} under NH$_3$ atmosphere. Finally, the product was washed in deionized water by ultrasonic for 30 min to dissolve the salt, then filtered and freeze-dried to obtain 2D layered W_2N_3 nanosheets.

2.2.2. Preparation of 1D CdS/2D W_2N_3

1D CdS/2D W_2N_3, which are denoted as CdS/W_2N_3 in this work, was synthesized by solvothermal reaction. In a typical procedure, a certain amount of above obtained 2D layered W_2N_3 nanosheets (10, 30, 50, 70, or 100 mg) was dispersed into 30 mL of ethylenediamine (EDA) with ultrasonication for 20 min by ultrasonic probe dispersion equipment. Then 2 mmol of Cd(Ac)$_2$·2 H_2O was added into the above-mixed suspension with gentle stirring at room temperature for 12 h. Subsequently, 20 mL of EDA solution of L-cysteine (4 mmol) was slowly dropped into the above-mixed suspension with stirring for 2 h. After that, the mixture was transferred into a 100 mL Teflon-lined autoclave, sealed, and maintained at 180 °C for 24 h. After cooled to room temperature, the precipitates were collected by centrifugation, the obtained samples were washed 3 times with deionized water and ethanol absolute, respectively, and dried in *vacuum* at 80 °C for 12 h. For clarity purposes, CdS/W_2N_3 prepared by using different amounts of W_2N_3 nanosheet samples were denoted as CW-1, CW-3, CW-5, CW-7, and CW-10, respectively. The specific content of W_2N_3 in CdS/W_2N_3 was obtained by XRF (Table S16). What's more, the same one-step solvothermal reaction without added Cd(Ac)$_2$·2 H_2O was done to verify the stability of W_2N_3 in solvothermal reaction, the sample was denoted as W_2N_3-H.

2.2.3. Preparation of 1D CdS nanowires

1D CdS nanowires were synthesized without added W_2N_3 nanosheets under the same method and conditions as preparation of 1D CdS/2D W_2N_3.

2.2.4. Preparation of CdS/Pt

The CdS/Pt composite was prepared by in situ photoreduction method. First, 20 mg CdS nanowires were ultrasonically dispersed in 80 mL 1 M FA aqueous solution. Then a certain amount of H$_2$PtCl$_6$·6 H_2O aqueous solution was dropwise added into the above CdS suspension solution in a Pyrex glass cell under continuous stirring. After that, the above suspension was deoxygenated with Ar for 20 min. Then formed ice cube was irradiated by Xe lamp for 2 h at room temperature. The sample was separated by centrifugation and dried in vacuum at 80 °C for 12 h.

2.2.5. Preparation of W_2N_3-NV and CdS/ W_2N_3-NV

More vacancies were introduced by annealing as-prepared W_2N_3 nanosheet under a hydrogen atmosphere. In detail, 100 mg of as-prepared W_2N_3 nanosheets were placed in the center of a tube furnace. Then the tube furnace was heated to 500 °C under 4% H$_2$/Ar atmosphere at a rate of 3 °C min^{-1}. The flow rate of the 4% H$_2$/Ar gas was 50 sccm. After maintaining the temperature of 500 °C for 4 h, the tube furnace was cooled to room temperature at a rate of 10 °C min^{-1}, the sample was denoted as W_2N_3-NV. CdS/W_2N_3-NV composites were synthesized under the same conditions as the preparation of 1D CdS/2D W_2N_3, where the amount of NV-W_2N_3 used was 50 mg.

2.3. Characterizations

The powder X-ray diffraction (XRD) patterns were obtained from a PANalytical X'pert MPD diffractometer operated at 40 kV and 40 mA using Ni-filtered Cu Kα irradiation (λ = 1.5406 Å). Field-emission scanning electron microscopy (FESEM) images were observed by a JEOL JSM-7800 F instrument. Transmission electron microscopy (TEM) images were obtained from an FEI Tecnai G^2 F30 S-Twin transmission electron microscope with an accelerating voltage of 300 kV. Energy dispersive X-ray spectrometer (EDX) was X-ray photoelectron spectra (XPS) were obtained on a Kratos Analytical Axis Ultra DLD instrument with a monochromatized Al Kα line source (150 W). All binding energies were referenced to the C 1 s peak at 284.8 eV. UV–vis absorption spectra (UV–vis) were measured on an Agilent Cary 5000 instrument equipped with a diffuse-reflectance accessory and with BaSO4 as the reference. Photoluminescence spectra (PL) analysis was carried out on a PTI

QuantaMaster 40 steady-state fluorescence spectrophotometer at room temperature with a solid-state sample. Thermogravimetric analysis (TGA) data was recorded on Netzsch-Gerätebau GmbH-STA 449 C Jupiter in an air atmosphere from room temperature to 1173 K with a heating rate of 10 K min^{-1}. The amounts of W_2N_3 in the samples were measured by X-ray fluorescence analysis (XRF, S4 PIONEER). The electron paramagnetic resonance (EPR) measurements were conducted by a Bruker A300–9.5/12. The samples were irradiated in the cavity of the EPR spectrometer with a Xe lamp. Femtosecond transient absorption (fs-TA) spectra were collected on a commercial femtosecond Ti/Sapphire regenerative amplifier laser system (Mai Tai, SOLSTICE ACE100F1K, Spectra-physics, 800 nm, <120 fs, 1.78 mJ, 1 KHz) and a data acquisition transient absorption spectrometer (Transpec-FS, CISS). The white-light continuum from 420 to 780 nm was generated by using 15% of the amplified 800 nm pulse into a Ti/Sapphire crystal, and the left 85% of the amplified 800 nm pulse was applied to generate the 400 nm pump pulse by an optical parameter amplifier (TPR-TOPAS-F, Spectra-physics). A 2 mm cuvette was used for all measurements.

2.4. Evaluation of photocatalytic performance

Photocatalytic reforming of formic acid was performed in a home-made reaction system. In detail, a certain amount of photocatalyst and 80 mL FA aqueous solution were mixed into a Pyrex glass cell (105 mL) with a side window for external light incidence and kept ultrasonic for at least 10 min. Then, the system was deoxygenated with Ar for 20 min. After that, the cell was irradiated by using Xenon lamp source (Micro-solar 300, Beijing Perfectlight) equipped with AM 1.5 G filter as the light source. The intensity of light was about 0.69 W·cm^{-2} in this work. Stirring was maintained throughout the photocatalytic reaction process. Cooled circulating water was used to maintain the reaction system at

room temperature (298.15 K). The volume of produced gas was obtained by an inverted graduated cylinder filled with silicone oil. The produced H_2, CO, and CO_2 were measured by a gas chromatograph equipped with a thermal-conductivity detector (Agilent 7890 A gas chromatograph with Ar as carrier gas). The type of chromatographic column used was PLOT C-2000. The translation of the instrument signal to specific amounts of H_2, CO, and CO_2 was determined by the external standard method. The cycling stability test experiment was performed by bubbling with Ar to refresh the reaction system.

3. Results and discussion

3.1. Synthesis and structural characterization of CdS/W$_2$N$_3$

To achieve high activity for photoreforming of formic acid, we designed 1D CdS/2D W_2N_3 composite photocatalysts. W_2N_3 nanosheets were prepared by a catalytic molten salt method [35]. The scanning electron microscopy (SEM) and transmission electron microscopy (TEM) images showed an obvious two-dimensional morphology of the as-prepared sample (Fig. S1a and Fig. 1a), and the X-ray diffraction (XRD) pattern indicated a similar crystal structure as that of h-W_2N_3 (Fig. 1c) [35–37]. Furthermore, the atomic structure of a hexagonal molecular phase was observed in high-resolution TEM (HRTEM) image (Fig. 1b), with an in-plane crystal lattice of 0.250 nm indexed to the (100) planes of h-W_2N_3 [38,39]. Moreover, the molar ratio of N: W was estimated as 1.78 ± 0.07 from thermo gravimetric analysis, which is in line with previous reports [37], thereby further confirming the successfully synthesized W_2N_3 nanosheets.

1D CdS/2D W_2N_3 composites with different mass ratios were subsequently prepared by solvothermal reaction. Diffraction peaks of CdS and W_2N_3 could be identified in the composite photocatalysts of CdS/
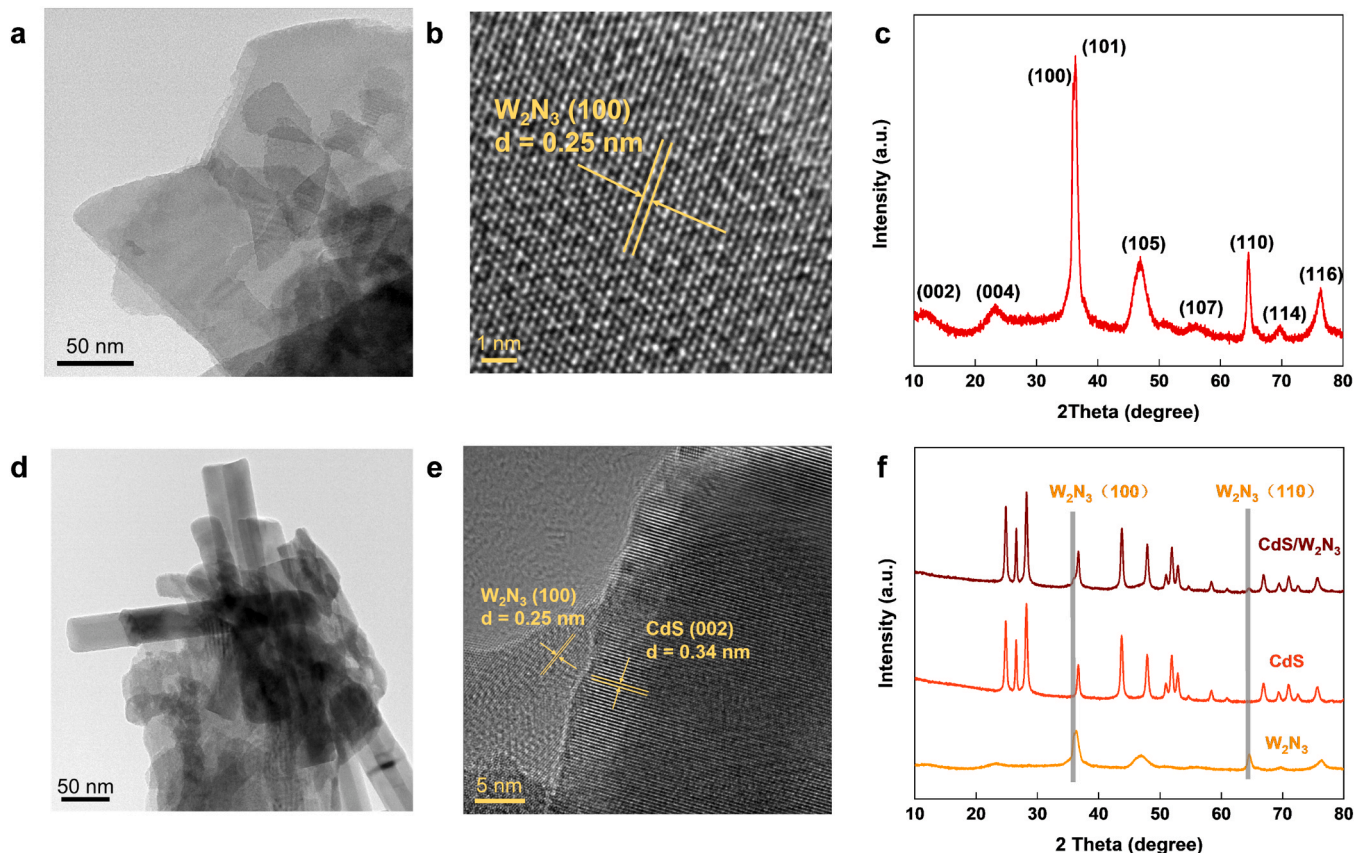

Fig. 1. Characterization of the W_2N_3 and CdS/W_2N_3 sample. TEM image (a) and HRTEM image of W_2N_3 sample (b). c, XRD pattern of W_2N_3 sample. TEM image (d) and HRTEM image of CdS/W_2N_3 sample (e). f, XRD pattern of CdS, W_2N_3, and CdS/W_2N_3 sample.

W_2N_3 (CW-5) [27,36], as indicated by the labeled (100) and (110) peaks of W_2N_3 at 36.0° and 64.5° (Fig. 1f). Combined with the analysis of TEM, SEM, and elemental mapping images of the composites (Fig. 1d, Fig. S1, S2, and S3), a composite of one-dimensional and two-dimensional materials, with CdS nanorods loaded on W_2N_3 nanosheets, was demonstrated. HRTEM image further indicated the intimate contact between the two components, in which the lattice spacings of 0.250 and 0.336 nm corresponding to the (100) and (002) planes of W_2N_3 nanosheets and CdS nanowires [39,40], respectively (Fig. 1e). Additionally, TEM image and XRD patterns confirmed the two-dimensional structure and crystal structure were retained after the solvothermal reaction (Fig. S4), indicating the excellent stability of W_2N_3 that could contribute to the improved activity and tuned selectivity in the following discussion.

3.2. Photoreforming of formic acid on CdS/W_2N_3 photocatalysts with high efficiency and tunable selectivity

To evaluate the performance of the CdS/W_2N_3 composite photocatalyst for FA photoreforming, we carried out the experiments under simulated sunlight at room temperature. H_2 and CO_2 were produced simultaneously during the reaction (Table S1) as dehydrogenation of FA occurred. The ratios of H_2/CO_2 were above the theoretical 1:1 stoichiometry due to the higher solubility of CO_2 in FA aqueous compared with

H_2. Notably, control experiments demonstrated that H_2, CO, CO_2, and other gas products were hardly detectable in the absence of either FA, light, or CdS (Table S1), indicating that the reaction in this work was indeed reforming of formic acid driven by CdS under irradiation. According to the results of the chopped-light linear sweep voltammograms and UV–visible (UV–vis) spectra (Fig. S5), there were no photocurrent responses of W_2N_3 under irradiation and no obvious changes in the absorption edge between CdS and CdS/W_2N_3, indicating that the photogenerated carriers were generated by CdS and W_2N_3 potentially acted as a cocatalyst in the system. Thereinto, as shown in Fig. 2a and Table S1, the H_2 production performance from FA reforming was boosted on CdS/W_2N_3 photocatalytic system. In particular, CW-5 provided a remarkable H_2 production of 408.90 μmol·h^{-1} in 1.0 M FA aqueous solution, exceeding that of bare CdS by a factor of 20. Further increasing the content of W_2N_3 led to decreased efficiency, due to the shade effect of excess W_2N_3 (Fig. S5b). Furthermore, the optimization experiment of FA concentration showed the H_2 production rate of 674.98 μmol·h^{-1} was obtained at 8.0 M FA (Fig. 2b and Table S2).

The above results demonstrated that 1D CdS/ 2D W_2N_3 prepared in this work could extremely promote the hydrogen evolution reaction (HER) in FA photoreforming via dehydrogenation process. Furthermore, it is interesting to note that beyond H_2 production, CO could also be detected in the gas products, indicating that the FA dehydration process also took place during FA photoreforming (details will be discussed
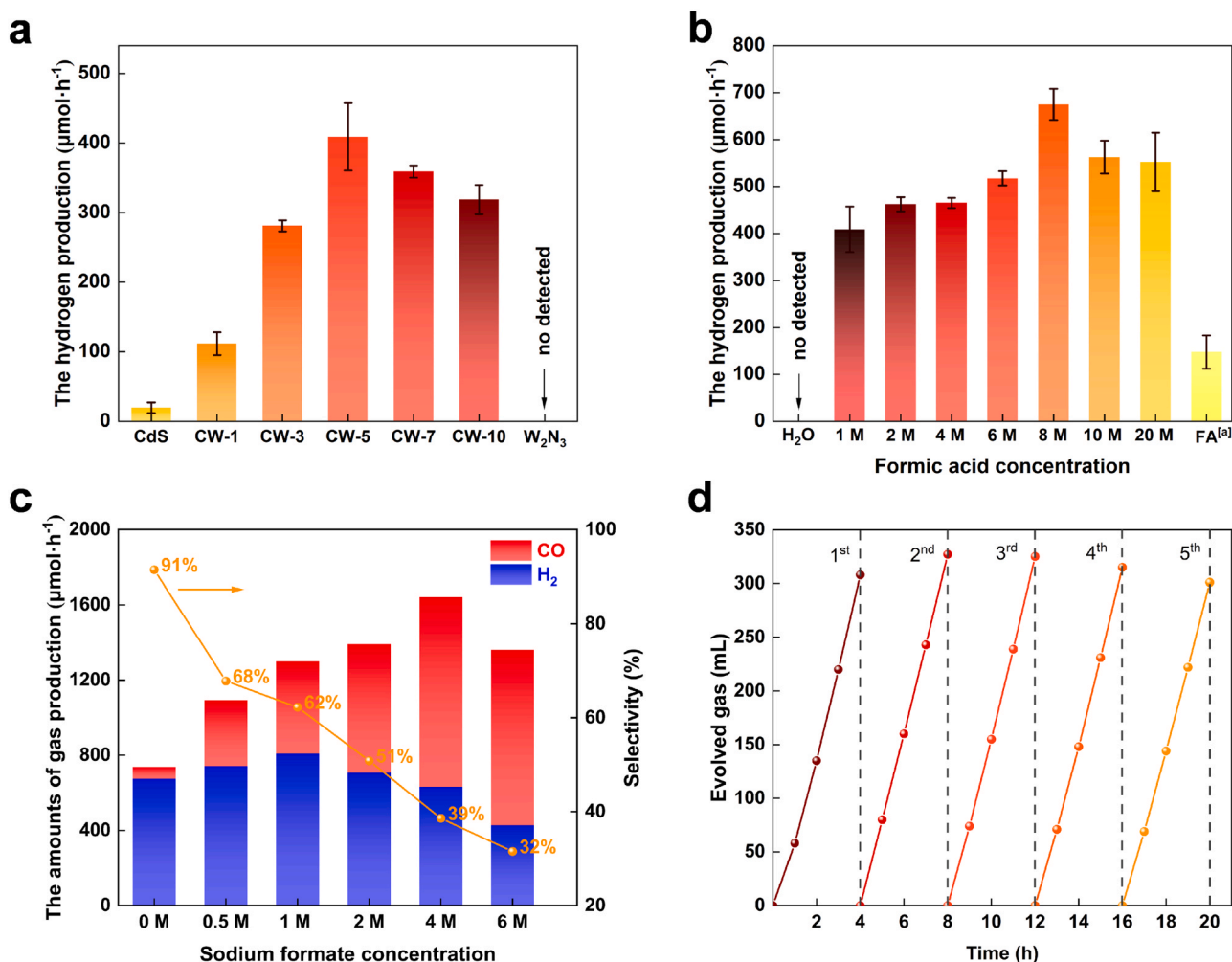

Fig. 2. Photocatalytic measurements for photoreforming of FA. (a) H_2 evolution with different CdS/ W_2N_3 samples in 1.0 M FA aqueous solution. (b) H_2 evolution with different FA concentrations. [a] formic acid (HCOOH, ≥98%, analytical grade). (c) Gas production with different sodium formate concentrations in 8.0 M FA aqueous solution. (d) The cycling stability test of CdS/ W_2N_3 (CW-5). Experiments in (a), (b), and (c) are conducted in 80 mL of solution with 4 mg of catalyst, and the experiments in (d) are conducted with 12 mg of catalyst.

later), and the CO production rate was also similarly enhanced in CdS/W_2N_3 composite photocatalyst (Table S1 and Table S2). What's more, the activity of FA photoreforming was greatly improved (Fig. 2c) when sodium formate (SF) was added to the photocatalytic reaction system as a common addition [14]. Thus, we tried two strategies for adding SF to the system. The results indicated the complex influence of FA and SF concentration on the photoreforming of FA (Fig. 2c and Fig. S6, Table S3 and Table S 4, more details were discussed in Supplementary Information), but the reacting system with CdS/W_2N_3 as the photocatalyst could achieve a wide range of selectivity control, such as the H_2 selectivity from almost 100% (20.0 M FA) to 31.5% (8.0 M FA and 6.0 M SF), which promised a more flexible application for photoreforming of FA to produce H_2 or syngas with tunable ratio CO/H_2 (0–2.18). Upon optimizing the concentration of catalyst (Fig. S7, Table S5) [41], FA, and SF, the maximum value of H_2 production rate of 329.20 µmol·mg^{-1}·h^{-1} was obtained at 7.0 M FA (1.0 SF) with 2 mg catalyst (Fig. S7a). The corresponding turnover frequency (TOF) was 724.92 h^{-1} (based on W_2N_3, Fig. S8a), and the activation energy (E_a) calculated based on the Arrhenius equation was 11.4 kJ·mol^{-1} (Fig. S8b). The apparent quantum yield (AQY) for H_2 production was estimated up to 61% at 420 nm, which is higher than previously reported values for photocatalytic FA dehydrogenation systems (Table S6). Moreover, corresponding to the above reaction conditions for the maximum value of H_2 production rate,

CO production rate could also reach a high value of 181.91 µmol·mg^{-1}·h^{-1}. It is worth noting that obvious gas bubbles could be observed by the naked eye even under outdoor sunlight irradiation (Video S1). The results of cycling test showed only a slight decrease of photocatalytic activity after 5 cycles, suggested remarkable stability of the as-established photocatalytic system for FA reforming (Fig. 2d and Fig. S9).

Supplementary material related to this article can be found online at doi:10.1016/j.addma.2020.101681.

3.3. Origin of efficient photoreforming of formic acid over CdS/W_2N_3

To further understand the reason for excellent FA photoreforming on CdS/W_2N_3, detailed characterizations on W_2N_3, CdS, and CdS/W_2N_3 were conducted. UV–vis spectra of CdS/W_2N_3 composites showed a similar light absorption edge with that for CdS (Fig. S5b), confirming the utilization range of optical spectrum by CdS and CdS/W_2N_3 is identical, suggesting the light absorption is not the reason for the significant difference in photocatalytic activity. Valance-band spectrum from X-ray photoelectron spectroscopy (XPS) (Fig. 3a) demonstrated the metallic properties of W_2N_3 with a finite electronic density of state (DOS) at the Fermi level (0 eV), which originates mostly from 5d electrons of W and 2p electrons of N and suggest that the metallic features of synthesized
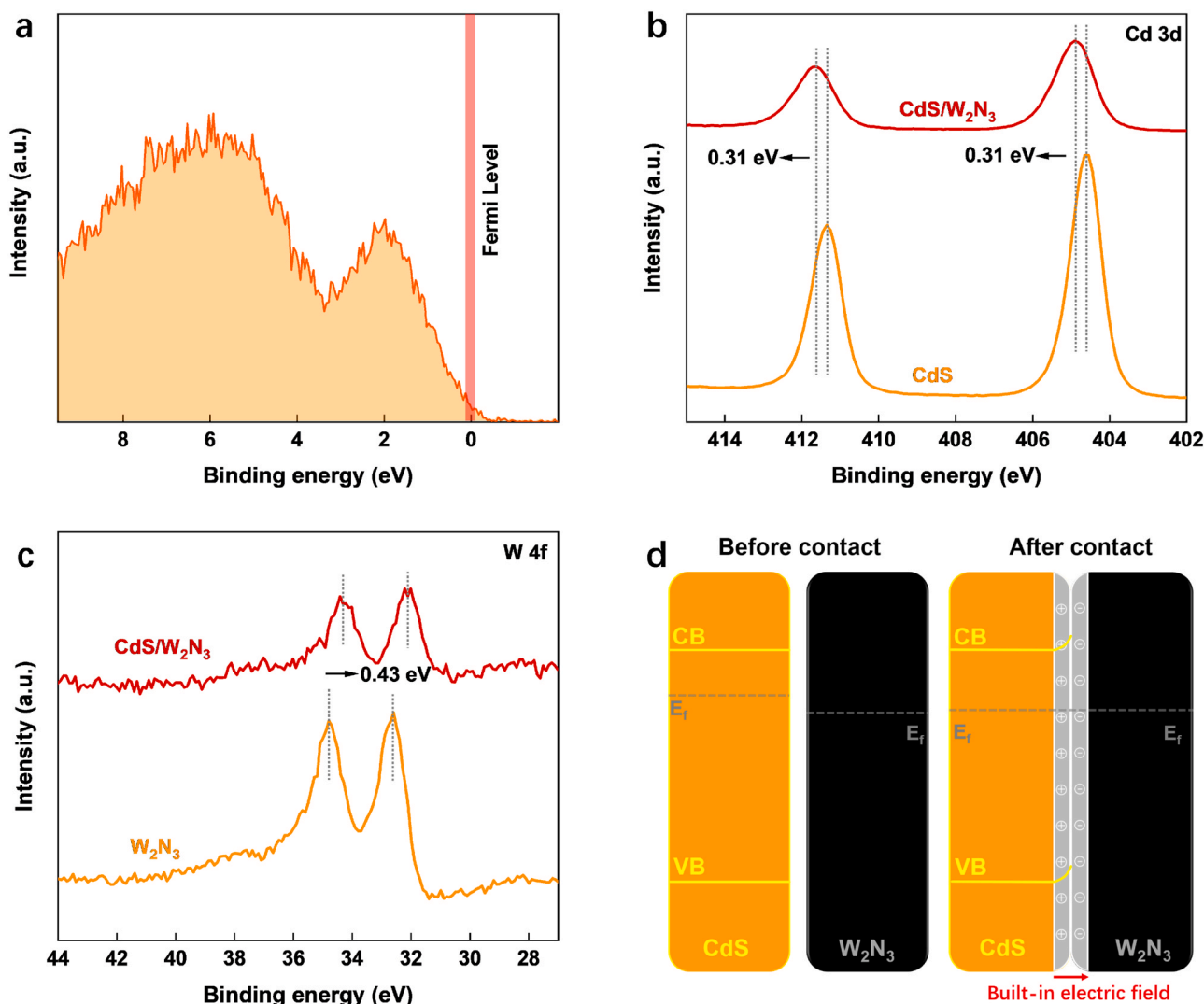

Fig. 3. Construction of CdS/W_2N_3 heterojunction. (a) Valence-band XPS spectrum of W_2N_3. (b) High-resolution XPS Cd 3d spectra of CdS and CdS/W_2N_3. (c) High-resolution XPS W 4 f spectra of W_2N_3 and CdS/W_2N_3. (d) Schematic illustration of as-established heterojunction between W_2N_3 and CdS.

W_2N_3 contributed to the excellent catalytic performance [37,42,43]. Meanwhile, according to the ultraviolet photoelectron spectroscopy (UPS), the work function of W_2N_3 was calculated to be 4.00 eV while 3.70 eV for CdS (Fig. S10). The different value of work function of CdS and W_2N_3 means when CdS is in contact with W_2N_3, electrons could be transferred from CdS with a lower work function (higher Fermi level) to W_2N_3 with a higher work function (lower Fermi level), thereby forming a strong interaction (Fig. 3d), similar to a Schottky junction [44]. Furthermore, as shown in the XPS spectra of Cd 3d and W 4 f (Fig. 3b and c), compared with the bare CdS and W_2N_3 samples, the Cd 3d peaks and the W 4 f peaks in CdS/W_2N_3 were positively shifted by 0.31 eV and negatively shifted by 0.43 eV, respectively, indicating the surface electron density of CdS decreased and that of W_2N_3 increased in the CdS/W_2N_3 composites. These above results imply the electrons transferred from CdS to W_2N_3 and confirm the strong interaction formatted between CdS and W_2N_3 in the composite, which facilitates separation of photogenerated carriers (Fig. 3d) [23,40,45,46]. As shown in Fig. S11 and S12, upon in-situ photodeposition experiments, the Au nanoparticles and MnO_x were found to be selectively localized on W_2N_3 and CdS, respectively. Due to the location of Au and MnO_x unveil the reduction and oxidation active sites, respectively, further indicating the photogenatrated electron would transfer to the W_2N_3 from CdS and the W_2N_3 would be as reduction active sites in photocatalytic reaction.

Charge-transfer properties in CdS/W_2N_3 heterojunction were further studied. As shown in Fig. 4a, the emission of photoillumenesense (PL) in the CdS/W_2N_3 was dramatically inhibited than that in the CdS, indicating rapid migration of photo-generated charge carriers, promoted in CdS/W_2N_3 heterojunction. Furthermore, transient absorption spectra (TAS) data was collected to probe the effect of the heterojunction on carrier transfer in the as-established photocatalytic system. Based on the related fit parameters (Fig. 4b, Table S7), the decay kinetics is faster in CdS/W_2N_3 (560.6 ps) than that in CdS (1754.2 ps), suggesting efficient electron transfer from CdS to W_2N_3 and again demonstrating the CdS/W_2N_3 heterojunction can improve the carrier transfer rates in photocatalytic systems. Moreover, open-circuit photovoltage (Voc) decay (OCPVD) measurement was conducted to evaluate the recombination rate of the photogenerated charge carriers. As shown in Fig. 4c, when the photoanodes were irradiated, the Voc of both CdS and CdS/W_2N_3 photoanodes showed a negative shift because the photogenerated electrons accumulated in the photoanode, while gradually decayed to the original level since the accumulated electrons would be redistributed due to charge recombination upon turning off the light [47]. It could be seen that the OCPVD process of CdS/W_2N_3 photoanode was slower than that of CdS photoanode, indicating that the recombination kinetics in CdS/W_2N_3 are moderate [48]. The lifetime of photogenerated electrons could be calculated from the Voc decay rate as shown in Fig. 4d. It was obvious that the electrons' lifetime of CdS/W_2N_3 photoanode was longer than that of CdS photoanode, indicating a slower recombination rate of photogenerated charge carriers due to efficient charge separation in CdS/W_2N_3. The above results all confirmed that constructing CdS/W_2N_3 heterojunctions have promoted the transfer and separation of photogenerated charge carriers, thereby enhancing the photocatalytic activity.

In addition to the above-mentioned carrier kinetic aspects, the adsorption and desorption of reactants in the catalyst has a great influence on the activity of the reaction. The further DFT analysis demonstrated that the molecule of FA could be chemically absorbed on the surface of {001} facet and {110} facet of W_2N_3 exothermically (Table S8 and Fig. 4e). In contrast, the {100} facet is not suitable for FA adsorption due to the endothermic adsorption process. Notably, the {001} facet of W_2N_3 has smoother energy changes for the adsorption of FA. Considering formate and protons will participate in the subsequent reactions (the detailed reaction mechanism will discuss in below section), the {001} facet could favor for the proton and formate desorption from the W_2N_3 to participate in the redox reaction due to the overtight interaction between formate and the {110} facet. In addition, the {001}

facet of W_2N_3 is more suitable for the adsorption and dissociation of FA to produce formate and protons than CdS, due to its smaller energy barrier of 0.03 eV (Table S9 and Fig. 4e). Those results indicated that the W_2N_3 could provide abundant active sites for FA dissociation, thus promoting photocatalytic reforming of formic acid activity.

3.4. Mechanism investigation of tuned selectivity and efficiency evaluation

As the previous investigation demonstrated boosted production of both H_2 and CO through as-established 1D/2D heterojunction with CdS as light absorber and W_2N_3 as cocatalyst. However, the results that the photocatalytic system was weakly active in FA solution and even inactive in pure water (Fig. 2b), it is suggested that both H_2O and FA molecules could not easily participate in the photocatalytic reaction reported here alone. To further confirm whether water participates in the reaction, the studies of the kinetic isotope effect and the mass spectrometry measurement in a solution of FA/H_2O versus FA/D_2O were introduced. The photocatalytic activity in deuterated solvent was only slightly lower than that in aqueous solution ($K_H/K_D = 1.14 \pm 0.10$), indicating the cleavage/formation of an O-H/ H-H bond with H atoms from H_2O, is not rate-limiting. Analysis of the hydrogen products in the FA/D_2O reaction system showed that H_2 was the dominant product, while only a very small amount of HD and D_2 was detected (Fig. S13), indicating that the reduction of H^+ from water dissociation is not the dominating HER reaction in as-established photocatalytic system. Therefore, it could be deduced that efficient FA photoreforming for H_2 production could only be obtained when effective dissociation of FA into H^+ and $HCOO^-$ is realized with the existence of water molecules in aqueous solution.

More evaluations were conducted to discover the photocatalytic reaction process of FA reforming with tunable selectivity. First, the active species for oxidation half-reaction were studied. The intermediate products of the reaction with electron paramagnetic resonance (EPR) measurements (Fig. S14a) showed that DMPO–$^\bullet CO_2^-$ ($a_N = 1.54$ mT, $a_{\beta-H} = 1.86$ mT) could be detected in FA aqueous solution with CdS/W_2N_3 photocatalyst under irradiation[49], implying that carbon dioxide radical anion ($CO_2^{\bullet-}$) is produced as the main intermediate product during the reaction. However, for CdS/W_2N_3 complexes, it was hard to detect any significant DMPO adduct signal in both pure water and FA solution ($\geq$98 wt%, AR) under irradiation (Fig. S14b and c). More detailed EPR measurements were conducted to study the intermediate product of FA photoreforming. Fig. S15 presents the EPR spectrum of CdS and W_2N_3 in FA aqueous solution, respectively. The results showed that there was no significant signal for W_2N_3 with or without irradiation, while the DMPO–$^\bullet CO_2^-$ signal was detected for CdS under light conditions, suggesting the $CO_2^{\bullet-}$ could be produced by CdS in CdS/W_2N_3 composite in the photoreforming of FA. To our best knowledge, the $CO_2^{\bullet-}$ could be formed by two possible mechanisms: 1) the $HCOO^-$ anion is oxidized to $CO_2^{\bullet-}$ by the photogenerated holes [50]; 2) the CO_2 dissolved in the liquid phase is reduced by the photogenerated electrons [51]. According to the EPR spectra of the photoreforming of FA in CdS/Pt system (H_2 selectivity is 100%) in which the photogenerated electrons were all utilized to reduce H^+ to H_2 (Table S10), the signal of DMPO–$^\bullet CO_2^-$ was also detected (Fig. S16), indicating the $CO_2^{\bullet-}$ could be formed by oxidizing $HCOO^-$ anion in the CdS system, which is also consistent with the oxidation ability of the photogenerated holes of CdS [27]. Whereas the electrons of CdS do not have a sufficient reduction ability to translate CO_2 to $CO_2^{\bullet-}$ (Fig. S17) [51,52]. Furthermore, the results of inhibition experiments indicated that it is the photogenerated holes, rather than $\bullet$OH radicals, that play an important role of active species in the photocatalytic reaction of CdS/W_2N_3 composite (Table S11). The above results suggested that $CO_2^{\bullet-}$ could be mainly generated from $HCOO^-$ oxidation by photogenerated holes. Thus, the photocatalytic mechanism for FA dehydrogenation (HCOOH→H_2 +CO_2) is proposed as follows: The H^+ that comes from HCOOH participates in

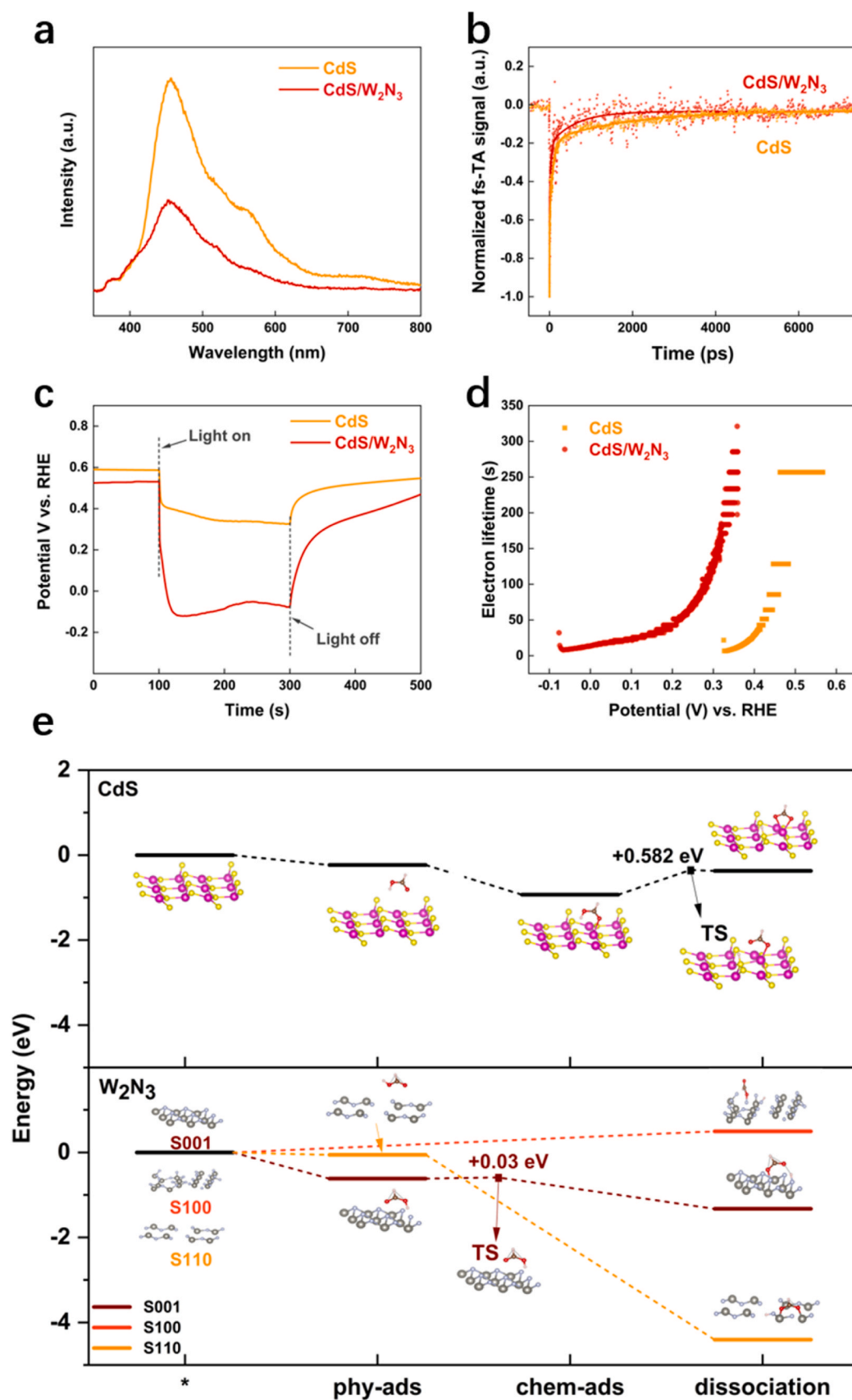**Fig. 4.** Charge-transfer properties. (a) Steady-state PL spectra for CdS and CdS/W$_2$N$_3$. (b) TA kinetic traces for CdS and CdS/W$_2$N$_3$ at 500 nm. (c) Open circuit potential vs. time profile of CdS and CdS/W$_2$N$_3$ photoanodes. (d) Electron lifetime for CdS and CdS/W$_2$N$_3$ are determined by the decay of open circuit potential after light off. (e) DFT calculated energy diagram of FA adsorbing on different crystal surfaces of W$_2$N$_3$ and the CdS {100} facet.

H_2 evolution reaction driven by photogenerated electrons accumulated on W_2N_3 cocatalyst, and the $HCOO^-$ anion is oxidized by the photogenerated holes from CdS to generate $CO_2^{\bullet-}$ and further oxidized to CO_2 (Scheme 1, equations 1–5). As such, it was also demonstrated that spatial separation of reduction and oxidation active sites was realized respectively on W_2N_3 and CdS for efficient FA reforming, as depicted in Scheme 1.
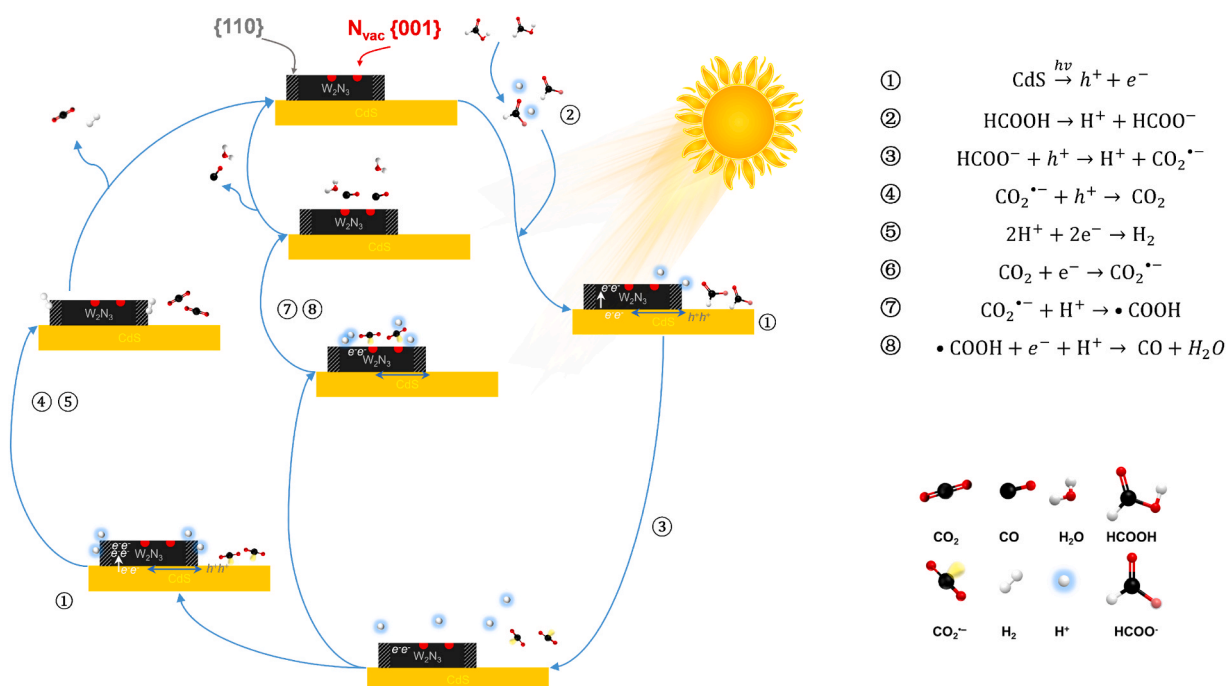
As for CO production, there are also two possible paths in the as-established photocatalytic system. One is the FA dehydration reaction with $CO_2^{\bullet-}$ as intermedia reactants (Equation 7–8), and the other is the reduction of CO_2 to CO (Equation 6–8) since both the $CO_2^{\bullet-}$ and dissolved CO_2 are possible reactants in the photocatalytic reduced reaction for CO generation. However, considering the solubility of CO_2 and the controlled experimental results for CO_2 photoreduction (Table S12), it is more likely that only a very limited proportion of the CO produced in this work is produced by direct reduction from CO_2. The reaction path with $CO_2^{\bullet-}$ as intermedia reactant is thus demonstrated as the dominating reaction via FA dehydration reaction. Considering that the valence of carbon element in CO is lower than that in $CO_2^{\bullet-}$, we suggest that CO production is also a single-electron photoreduction process (FA dehydration as in Equations 1–3, 7, and 8) with active sites also located on W_2N_3 of CdS/W_2N_3 composite. It is worth noting that the contribution of the reaction ($2CO_2^{\bullet-} + 2H^+ \rightarrow CO_2 + CO + H_2O$) [28], which produces gas with a theoretical CO/H_2 value of 1:1, is considered small in this photocatalytic system. This is because, under some conditions, the CO/H_2 ratio in the gas produced by the reaction system is significantly larger than 1 (Table S3).

Beyond that, it is more important to clarify the origin of tuned selectivity between H_2 and CO. It is interesting to note that beyond lattice N, the signal of nitrogen vacancy (N-vacancy) at ~399.7 eV could be observed in N 1 s XPS spectrum of W_2N_3 (Fig. 5a) [36,39]. The N-vacancies are considered to be unavoidable intrinsic defects arising from the material synthesis process. As suggested by Density functional theory (DFT) calculations, due to N-vacancies, subsurface W atoms are exposed and an electron-deficient area is produced (Fig. 5c). Consequently, the N-vacancies as a Lewis acid site may be an active reactive site [53], suggesting the unpaired electron in negatively charged $CO_2^{\bullet-}$ could be accommodated at the charge depletion area [54–56]. As shown

in Fig. S19b and c, $CO_2^{\bullet-}$ is adsorbed on perfect W_2N_3 via surface van der Waals interaction, and no obvious charge transfer exists among this physical adsorption structure. However, when N vacancy is involved, the $CO_2^{\bullet-}$ could be adsorbed on W_2N_3 with significant charge transfer (Fig. 5d, S19d-c). This indicates that N vacancies could facilitate the adsorption and activation of the $CO_2^{\bullet-}$ by acting as potential active sites. Furthermore, after increasing the N vacancies in W_2N_3 (W_2N_3-NV, Fig. 5b, Supplementary Information), the selectivity for CO production correspondingly increased (Table S13), further confirming that the N vacancies have a major effect on the reaction of CO evolution.

Moreover, the free energy change of the rate-limiting step for CO evolution reaction (CER) on different surfaces was studied (Fig. 5e, Table S14). The {001} facet with N vacancies owns the smallest free energy change among all the surfaces, further suggested being more favorable for CER than other facets. That means further nitrogen-vacancy-engineering could be another method to achieve controllable selectivity for photoreforming of FA in CdS/W_2N_3 composite systems in the future, even possible for other transition metal nitride (TMN) groups. Notably, the {001} facet with N vacancies in W_2N_3 is considered to have poor HER activity [57]. As DFT calculations suggested, the {110} facet of W_2N_3 is more suitable for HER, in which the adsorption and desorption processes can take place easily (Fig. 5f and S20, Table S15, more detailed discussion in SI). The above results suggest that the active sites of HER and CER are not only different but also spatially separated, which may be favorable for the two reactions to proceed independently. However, the dehydrogenation (for H_2 production) and dehydration (for CO production) reactions in the FA photocatalytic reforming reaction are still in competition with each other (Scheme 1), since both of them consume photogenerated electrons. Accordingly, the mechanism of as-achieved tunable selectivity by controlling the concentration of SF and FA in the reaction system could be proposed as follows:

The decline of H^+ concentration and the increment of $HCOO^-$ concentration are committed with the addition of SF. As such, the lower H^+ concentration is not favorable for hydrogen evolution reaction (HER), while the higher $HCOO^-$ concentration facilitates the oxidation reaction in the photocatalytic reaction, thereby increasing the concentration of $CO_2^{\bullet-}$ intermediate for further facilitating the CER (first three trials in

① $CdS \xrightarrow{h\nu} h^+ + e^-$

② $HCOOH \rightarrow H^+ + HCOO^-$

③ $HCOO^- + h^+ \rightarrow H^+ + CO_2^{\bullet-}$

④ $CO_2^{\bullet-} + h^+ \rightarrow CO_2$

⑤ $2H^+ + 2e^- \rightarrow H_2$

⑥ $CO_2 + e^- \rightarrow CO_2^{\bullet-}$

⑦ $CO_2^{\bullet-} + H^+ \rightarrow \bullet COOH$

⑧ $\bullet COOH + e^- + H^+ \rightarrow CO + H_2O$

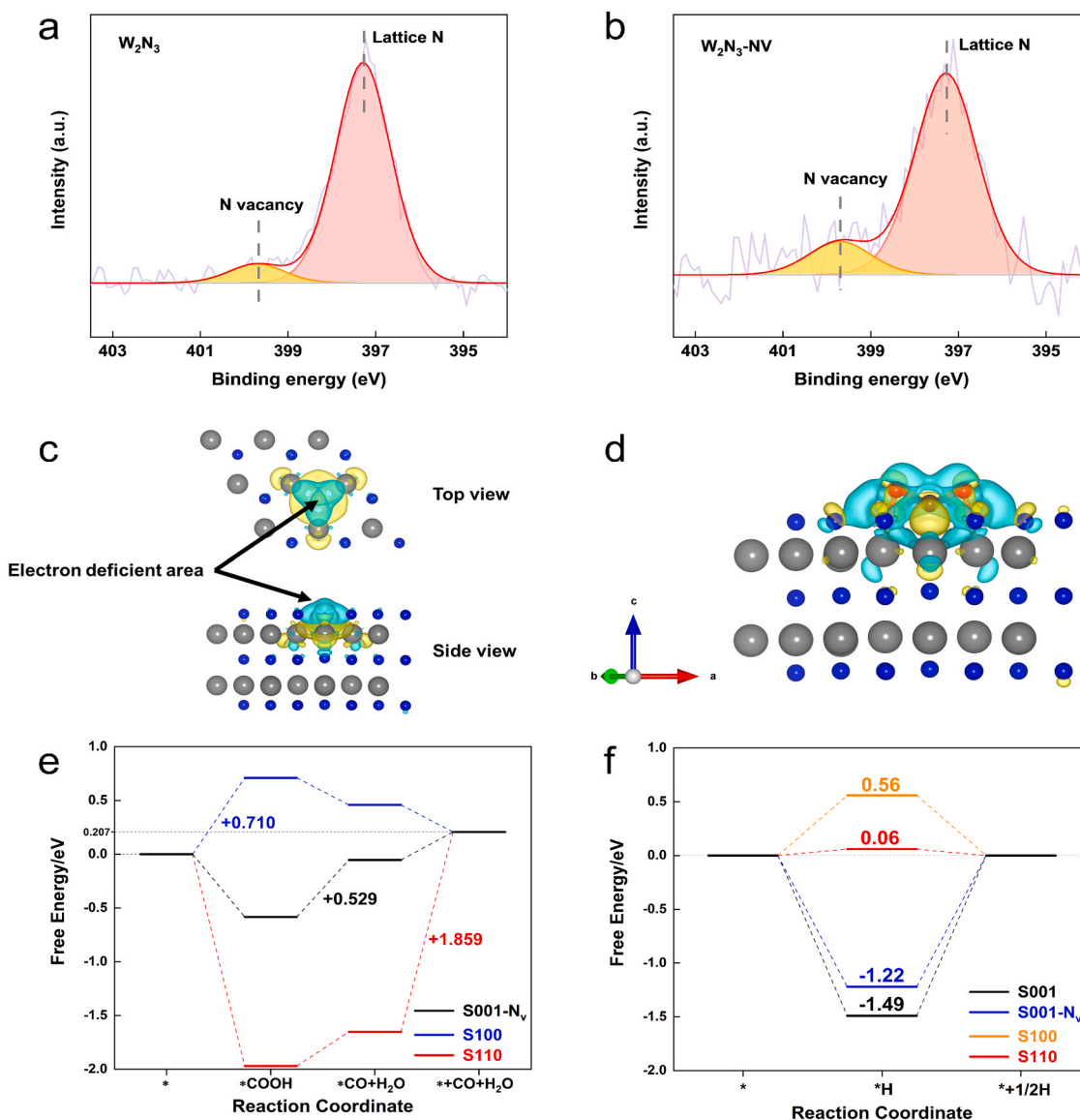**Scheme 1.** Mechanism of CdS/W_2N_3 for photoreforming of formic acid.

Fig. 5. XPS spectrum of N 1 s of (a) W_2N_3 and (b) W_2N_3-NV. (c) Charge density difference induced by nitrogen vacancy on W_2N_3. (d) Views of interfacial electron transfer of $CO_2^{\bullet-}$ on W_2N_3 with N vacancy. The light blue and yellow color areas represent the electron deficiency and accumulation, respectively. The blue, grey, red, and brown color balls represent N, W, O, and C atoms, respectively. (e) Free energy diagram of different surfaces for CER. (f) The free energy diagram of H atom on different surfaces.

Table S3 and Fig. S6). However, excessively lowered H^+ concentration is detrimental to both CER (Equations 7 and 8) and HER (Equation 5), which is consistent with the experimental results (last three trials in Table S3 and Fig. S6). Therefore, CdS/W_2N_3 photocatalytic system is sensitive to proton concentration and formate concentration, thus making the controlled selectivity between H_2 and CO feasible in a wide range. Notably, assuming that all CO molecules were generated through a one-photon reaction, a minimum AQY for CO of 15.84% was recorded at a condition of maximum AQY for H_2 at 420 nm, and the total AQY of syngas was calculated as 76.84% ($AQY_{H2} + AQY_{CO}$), demonstrating the extremely high utilization of the photons within the absorbed solar irradiation for FA reforming in CdS/W_2N_3 photocatalytic system.

4. Conclusions

In summary, we developed a noble-metal-free and efficient photocatalytic system for solar-driven reforming of formic acid with controllable selectivity. 1D CdS/2D W_2N_3 heterojunction photocatalyst exhibited record-high hydrogen and carbon monoxide generation rate of

$329.20\ \mu mol \cdot mg^{-1} \cdot h^{-1}$ and $181.91\ \mu mol \cdot mg^{-1} \cdot h^{-1}$, respectively, in 7 M FA (1 M SF) aqueous solution at room temperature. The excellent photocatalytic performance originates from the construction of heterojunctions that facilitates the separation of charge carriers. In particular, the nitrogen vacancies in W_2N_3 contribute to the activation of intermediate $CO_2^{\bullet-}$, so that the selectivity of the reaction system can be controlled by optimizing reaction media, with the reforming product transformed from pure hydrogen to syngas with tunable ratios of CO/H_2. This work proposes a more flexible photocatalytic system by using low-cost transition metal nitrides as cocatalysts to efficiently produce renewable hydrogen energy and valuable chemical feedstock.

CRediT authorship contribution statement

Xiaoyuan Ye: Data curation, Formal analysis, Funding acquisition, Investigation, Methodology, Software, Validation, Visualization, Writing – original draft , Writing – review & editing. **Yuchen Dong:** Data curation, Formal analysis, Investigation, Software, Writing – review & editing. **Ziying Zhang:** Formal analysis, Software. **Wengao**

Declaration of Competing Interest

The authors declare that they have no known competing financial interests or personal relationships that could have appeared to influence the work reported in this paper.

Data Availability

Data will be made available on request.

Acknowledgements

Appendix A. Supporting information

Supplementary data associated with this article can be found in the online version at doi:10.1016/j.apcatb.2023.123073.

References

[1] F. Valentini, V. Kozell, C. Petrucci, A. Marrocchi, Y.L. Gu, D. Gelman, L. Vaccaro, Formic acid, a biomass-derived source of energy and hydrogen for biomass upgrading, Energy Environ. Sci. 12 (2019) 2646–2664.

[2] I. Dutta, S. Chatterjee, H. Cheng, R.K. Parsapur, Z. Liu, Z. Li, E. Ye, H. Kawanami, J. S.C. Low, Z. Lai, X.J. Loh, K.W. Huang, Formic acid to power towards low-carbon economy, Adv. Energy Mater. 12 (2022) 2103799.

[3] J. Cao, Z. Zheng, Z. Xu, L. Xu, Transition-metal-catalyzed transfer carbonylation with HCOOH or HCHO as non-gaseous C1 source, Coord. Chem. Rev. 336 (2017) 43–53.

[4] S. Zhai, S. Jiang, C. Liu, Z. Li, T. Yu, L. Sun, G. Ren, W. Deng, Liquid sunshine: formic acid, J. Phys. Chem. Lett. 13 (2022) 8586–8600.

[5] N. Kato, S. Mizuno, M. Shiozawa, N. Nojiri, Y. Kawai, K. Fukumoto, T. Morikawa, Y. Takeda, A large-sized cell for solar-driven CO2 conversion with a solar-to-formate conversion efficiency of 7.2%, Joule 5 (2021) 687–705.

[6] D. Antón-García, E. Edwardes Moore, M.A. Bajada, A. Eisenschmidt, A.R. Oliveira, I.A.C. Pereira, J. Warnan, E. Reisner, Photoelectrochemical hybrid cell for unbiased CO2 reduction coupled to alcohol oxidation, Nat. Synth. 1 (2022) 77–86.

[7] D. Wei, R. Sang, P. Sponholz, H. Junge, M. Beller, Reversible hydrogenation of carbon dioxide to formic acid using a Mn-pincer complex in the presence of lysine, Nat. Energy (2022) 438–447.

[8] F.M. Schwarz, J. Moon, F. Oswald, V. Müller, Biological hydrogen storage and release through multiple cycles of bi-directional hydrogenation of CO2 to formic acid in a single process unit, Joule 6 (2022) 1304–1319.

[9] L. Qi, Y.F. Mui, S.W. Lo, M.Y. Lui, G.R. Akien, I.T. Horvath, Catalytic conversion of fructose, glucose, and sucrose to 5-(Hydroxymethyl)furfural and levulinic and formic acids in gamma-Valerolactone as a green solvent, ACS Catal. 4 (2014) 1470–1477.

[10] D. Voß, H. Pickel, J. Albert, Improving the fractionated catalytic oxidation of lignocellulosic biomass to formic acid and cellulose by using design of experiments, ACS Sustain. Chem. Eng. 7 (2019) 9754–9762.

[11] C.Y. Toe, C. Tsounis, J. Zhang, H. Masood, D. Gunawan, J. Scott, R. Amal, Advancing photoreforming of organics: highlights on photocatalyst and system designs for selective oxidation reactions, Energy Environ. Sci. 14 (2021) 1140–1175.

[12] A.V. Puga, Photocatalytic production of hydrogen from biomass-derived feedstocks, Coord. Chem. Rev. 315 (2016) 1–66.

[13] A. Garcia-Baldovi, R. Del Angel, G. Mouachaham, S.-P. Liu, D. Fan, G. Maurin, S. Navalon, C. Serre, H. Garcia, Active site imprinting on Ti oxocluster metal-organic

framework for the photocatalytic hydrogen release from formic acid, Energy Environ. Sci., (2022).

[14] T. Wang, T. Yang, D. Jiang, H. Cao, A.C. Minja, P. Du, CdS nanorods anchored with crystalline FeP nanoparticles for efficient photocatalytic formic acid dehydrogenation, ACS Appl. Mater. Interfaces 13 (2021) 23751–23759.

[15] Y. Li, R. He, P. Han, B. Hou, S. Peng, C. Ouyang, A new concept: volume photocatalysis for efficient H2 generation - using low polymeric carbon nitride as an example, Appl. Catal. B Environ. 279 (2020).

[16] P. Zhou, Q. Zhang, Z. Xu, Q. Shang, L. Wang, Y. Chao, Y. Li, H. Chen, F. Lv, Q. Zhang, L. Gu, S. Guo, Atomically dispersed Co-P(3) on CdS nanorods with electron-rich feature boosts photocatalysis, Adv. Mater. 32 (2020), e1904249.

[17] Q. Zhang, Q. Mao, Y. Zhou, L. Zou, D. Zhu, Y. Huang, H. Gao, X. Luo, Y. Mao, Z. Liang, Study of non-noble-metal-based metal–nitrogen–carbon catalysts for formic acid dehydrogenation, ACS Sustain. Chem. Eng. (2022).

[18] D.A. Bulushev, M. Zacharska, A.S. Lisitsyn, O.Y. Podyacheva, F.S. Hage, Q. M. Ramasse, U. Bangert, L.G. Bulusheva, Single atoms of Pt-group metals stabilized by N-doped carbon nanofibers for efficient hydrogen production from formic acid, ACS Catal. 6 (2016) 3442–3451.

[19] W. Wang, Y. Tao, J. Fan, Z. Yan, H. Shang, D.L. Phillips, M. Chen, G. Li, Fullerene–graphene acceptor drives ultrafast carrier dynamics for sustainable CdS photocatalytic hydrogen evolution, Adv. Funct. Mater. 32 (2022) 2201357.

[20] Z. Ai, M. Huang, D. Shi, M. Yang, H. Hu, B. Zhang, Y. Shao, J. Shen, Y. Wu, X. Hao, Phase engineering of CdS optimized by BP with p-n junction: Establishing spatial-gradient charges transmission mode toward efficient photocatalytic water reduction, Appl. Catal. B Environ. 315 (2022), 121577.

[21] P. Zhang, D. Luan, X.W. Lou, Fabrication of CdS frame-in-cage particles for efficient photocatalytic hydrogen generation under visible-light irradiation, Adv. Mater. 32 (2020) 2004561.

[22] S. Fukuzumi, T. Kobayashi, T. Suenobu, Photocatalytic production of hydrogen by disproportionation of one-electron-reduced rhodium and iridium-ruthenium complexes in water, Angew. Chem. Int. Ed. Engl. 50 (2011) 728–731.

[23] Y.Y. Cai, X.H. Li, Y.N. Zhang, X. Wei, K.X. Wang, J.S. Chen, Highly efficient dehydrogenation of formic acid over a palladium-nanoparticle-based Mott-Schottky photocatalyst, Angew. Chem. Int. Ed. 52 (2013) 11822–11825.

[24] Y.X. Li, Y.F. Hu, S.Q. Peng, G.X. Lu, S.B. Li, Synthesis of CdS nanorods by an ethylenediamine assisted hydrothermal method for photocatalytic hydrogen evolution, J. Phys. Chem. C 113 (2009) 9352–9358.

[25] Z.Y. Zhang, S.W. Cao, Y.S. Liao, C. Xue, Selective photocatalytic decomposition of formic acid over AuPd nanoparticle-decorated TiO2 nanofibers toward high-yield hydrogen production, Appl. Catal. B Environ. 162 (2015) 204–209.

[26] L. Xiao, Y.-S. Jun, B. Wu, D. Liu, T.T. Chuong, J. Fan, G.D. Stucky, Carbon nitride supported AgPd alloy nanocatalysts for dehydrogenation of formic acid under visible light, J. Mater. Chem. A 5 (2017) 6382–6387.

[27] S. Cao, Y. Chen, H. Wang, J. Chen, X.H. Shi, H.M. Li, P. Cheng, X.F. Liu, M. Liu, L. Y. Piao, Ultrasmall CoP nanoparticles as efficient cocatalysts for photocatalytic formic acid dehydrogenation, Joule 2 (2018) 549–557.

[28] H. Zhou, M. Wang, F. Wang, Oxygen-controlled photo-reforming of biopolyols to CO over Z-scheme CdS@g-C3N4, Chem 8 (2021) 465–479.

[29] X. Hu, J. Jin, Y. Wang, C. Lin, S. Wan, K. Zhang, L. Wang, J.H. Park, Au/MoS2 tips as auxiliary rate aligners for the photocatalytic generation of syngas with a tunable composition, Appl. Catal. B Environ. 308 (2022), 121219.

[30] Z. Liang, L. Song, M. Sun, B. Huang, Y. Du, Tunable CO/H2 ratios of electrochemical reduction of CO2 through the Zn-Ln dual atomic catalysts, Sci. Adv. 7 (2021), eabl4915.

[31] S. Guo, S. Zhao, X. Wu, H. Li, Y. Zhou, C. Zhu, N. Yang, X. Jiang, J. Gao, L. Bai, Y. Liu, Y. Lifshitz, S.T. Lee, Z. Kang, A Co3O4-CDots-C3N4 three component electrocatalyst design concept for efficient and tunable CO2 reduction to syngas, Nat. Commun. 8 (2017) 1828.

[32] V. Andrei, B. Reuillard, E. Reisner, Bias-free solar syngas production by integrating a molecular cobalt catalyst with perovskite–BiVO4 tandems, Nat. Mater. 19 (2020) 189–194.

[33] M.F. Kuehnel, D.W. Wakerley, K.L. Orchard, E. Reisner, Photocatalytic formic acid conversion on CdS nanocrystals with controllable selectivity for H2 or CO, Angew. Chem. Int. Ed. 54 (2015) 9627–9631.

[34] R.M. Irfan, T. Wang, D. Jiang, Q. Yue, L. Zhang, H. Cao, Y. Pan, P. Du, Homogeneous molecular iron catalysts for direct photocatalytic conversion of formic acid to syngas (CO+H2), Angew. Chem. Int. Ed. Engl. 59 (2020) 14818–14824.

[35] H. Jin, Q. Gu, B. Chen, C. Tang, Y. Zheng, H. Zhang, M. Jaroniec, S.-Z. Qiao, Molten salt-directed catalytic synthesis of 2D layered transition-metal nitrides for efficient hydrogen evolution, Chem 6 (2020) 2382–2394.

[36] H. Jin, L. Li, X. Liu, C. Tang, W. Xu, S. Chen, L. Song, Y. Zheng, S.-Z. Qiao, Nitrogen vacancies on 2D layered W2N3: a stable and efficient active site for nitrogen reduction reaction, Adv. Mater. 31 (2019) 1902709.

[37] S. Wang, X. Yu, Z. Lin, R. Zhang, D. He, J. Qin, J. Zhu, J. Han, L. Wang, H.-K. Mao, J. Zhang, Y. Zhao, Synthesis, crystal structure, and elastic properties of novel tungsten nitrides, Chem. Mater. 24 (2012) 3023–3028.

[38] S. Tan, B.M. Tackett, Q. He, J.H. Lee, J.G. Chen, S.S. Wong, Synthesis and electrocatalytic applications of flower-like motifs and associated composites of nitrogen-enriched tungsten nitride (W2N3), Nano Res. 13 (2020) 1434–1443.

[39] Y. Lin, C. Yang, Q. Niu, S. Luo, Interfacial charge transfer between silver phosphate and W2N3 induced by nitrogen vacancies enhances removal of β-Lactam antibiotics, Adv. Funct. Mater. (2021).

[40] R. Xiao, C.X. Zhao, Z.Y. Zou, Z.P. Chen, L. Tian, H.T. Xu, H. Tang, Q.Q. Liu, Z. X. Lin, X.F. Yang, In situ fabrication of 1D CdS nanorod/2D Ti3C2 MXene nanosheet

Schottky heterojunction toward enhanced photocatalytic hydrogen evolution, Appl. Catal. B Environ. 268 (2020), 118382.

[41] S. Cao, L. Piao, Considerations for a more accurate evaluation method for photocatalytic water splitting, Angew. Chem. Int. Ed. 59 (2020) 18312–18320.

[42] Z. Cheng, W. Qi, C.H. Pang, T. Thomas, T. Wu, S. Liu, M. Yang, Recent advances in transition metal nitride-based materials for photocatalytic applications, Adv. Funct. Mater. (2021) 2100553.

[43] Y.L. Wang, T. Nie, Y.H. Li, X.L. Wang, L.R. Zheng, A.P. Chen, X.Q. Gong, H.G. Yang, Black tungsten nitride as a metallic photocatalyst for overall water splitting operable at up to 765nm, Angew. Chem. 129 (2017) 7538–7542.

[44] Y. Xu, C. Cheng, S. Du, J. Yang, B. Yu, J. Luo, W. Yin, E. Li, S. Dong, P. Ye, X. Duan, Contacts between two- and three-dimensional materials: ohmic, Schottky, and p–n heterojunctions, ACS Nano 10 (2016) 4895–4919.

[45] C.-Q. Li, S.-S. Yi, Y. Liu, Z.-L. Niu, X.-Z. Yue, Z.-Y. Liu, In-situ constructing S-scheme/Schottky junction and oxygen vacancy on SrTiO₃ to steer charge transfer for boosted photocatalytic H₂ evolution, Chem. Eng. J. 417 (2021), 129231.

[46] C. Zhou, S. Wang, Z. Zhao, Z. Shi, S. Yan, Z. Zou, A facet-dependent Schottky-Junction electron shuttle in a BiVO₄ {010}-Au-Cu₂O Z-Scheme photocatalyst for efficient charge separation, Adv. Funct. Mater. 28 (2018) 1801214.

[47] W.L. Fu, X.J. Guan, Y.T. Si, M.C. Liu, Phosphatized GaZnInON nanocrystals with core-shell structures for efficient and stable pure water splitting via four-electron photocatalysis, Chem. Eng. J. 410 (2021), 128391.

[48] H. Cui, G. Zhu, Y. Xie, W. Zhao, C. Yang, T. Lin, H. Gu, F. Huang, Black nanostructured Nb₂O₅ with improved solar absorption and enhanced photoelectrochemical water splitting, J. Mater. Chem. A 3 (2015) 11830–11837.

[49] J. Hu, H. Chen, X. Hou, X. Jiang, Cobalt and copper Iions synergistically enhanced photochemical vapor generation of molybdenum: mechanism study and analysis of water samples, Anal. Chem. 91 (2019) 5938–5944.

[50] C.M. Hendy, G.C. Smith, Z. Xu, T. Lian, N.T. Jui, Radical chain reduction via carbon dioxide radical anion (CO₂⁻), J. Am. Chem. Soc. 143 (2021) 8987–8992.

[51] L. Yuan, M.Y. Qi, Z.R. Tang, Y.J. Xu, Coupling strategy for CO₂ valorization integrated with organic synthesis by heterogeneous photocatalysis, Angew. Chem. Int. Ed. Engl. 60 (2021) 21150–21172.

[52] D. Friedmann, A. Hakki, H. Kim, W. Choi, D. Bahnemann, Heterogeneous photocatalytic organic synthesis: state-of-the-art and future perspectives, Green. Chem. 18 (2016) 5391–5411.

[53] S. Chen, B. Wang, J. Zhu, L. Wang, H. Ou, Z. Zhang, X. Liang, L. Zheng, L. Zhou, Y. Q. Su, D. Wang, Y. Li, Lewis acid site-promoted single-atomic Cu catalyzes electrochemical CO₂ methanation, Nano Lett. 21 (2021) 7325–7331.

[54] W. Wang, Y. Wang, R. Yang, Q. Wen, Y. Liu, Z. Jiang, H. Li, T. Zhai, Vacancy-rich Ni(OH)₂ drives the electrooxidation of amino C-N bonds to nitrile C identical with N bonds, Angew. Chem. Int. Ed. Engl. 59 (2020) 16974–16981.

[55] S. Kang, S. Han, Y. Kang, Unveiling electrochemical reaction pathways of CO₂ reduction to CN species at S-Vacancies of MoS₂, ChemSusChem 12 (2019) 2671–2678.

[56] J. Lee, S. Kang, K. Yim, K.Y. Kim, H.W. Jang, Y. Kang, S. Han, Hydrogen evolution reaction at anion vacancy of two-dimensional transition-metal dichalcogenides: Ab initio computational screening, J. Phys. Chem. Lett. 9 (2018) 2049–2055.

[57] X. Yang, J. Nash, J. Anibal, M. Dunwell, S. Kattel, E. Stavitski, K. Attenkofer, J. G. Chen, Y. Yan, B. Xu, Mechanistic insights into electrochemical nitrogen reduction reaction on vanadium nitride nanoparticles, J. Am. Chem. Soc. 140 (2018) 13387–13391.